High-Speed Contactless Sintering Characterization for Printed Electronics by Frequency-Domain Thermoreflectance

Md Saifur Rahman[1], Mohammadreza Shahzadeh[1], Mizanur Rahman[2], Simone Pisana[1,2], Gerd Grau[1]*

[1]Department of Electrical Engineering and Computer Science
Lassonde School of Engineering, York University
4700 Keele Street,
Toronto, ON, M3J 1P3, Canada

[2]Department of Physics and Astronomy
Faculty of Science, York University
4700 Keele Street
Toronto, ON, M3J 1P3, Canada

*Email: grau@eecs.yorku.ca

Abstract

Printed electronics is an alternative manufacturing paradigm for low-cost and large-area microelectronic devices and systems. Metal nanoparticle (MNP) inks are favorable to print conductors due to their high electrical conductivity. As-printed MNP ink requires sintering to become electrically conductive. High-quality MNP conductors require monitoring and optimization of the sintering process. Traditionally, electrical conductivity is measured to monitor the different sintering stages. This requires destructive probing or fabrication of dedicated test structures, which is challenging for in-line monitoring of high-volume manufacturing. Here, we demonstrate that frequency-domain thermoreflectance (FDTR), an optical pump-probe technique, can be used for process monitoring. Conductive features are inkjet printed with a silver nanoparticle ink. Intense pulsed light (IPL) sintering is used rather than traditional thermal sintering due to its capability of millisecond sintering. Thermal conductivity of IPL sintered features is measured using FDTR, where a frequency-modulated heat flux is applied with a pump laser and the obtained thermal phase of the probe laser is fitted to a thermal model. Thermal conductivity measured from FDTR agrees well with thermal conductivity calculated using Wiedemann-Franz Law from electrical conductivity measurements. By appropriately choosing six FDTR pump frequencies with the highest sensitivity and taking all the selected frequency-vs-phase data points at once, we can measure thermal conductivity in 12 s, a fraction of the traditional measurement time. In this way, the measurement time decreases considerably, and thermoreflectance becomes a suitable characterization technique for high-throughput manufacturing. A Monte Carlo based prediction was performed to observe the effect of shorter measurement time on phase noise, and a much faster measurement configuration is proposed with an acceptable uncertainty in measurement. Our results demonstrate a simple approach for high-speed non-contact characterization of metal nanoparticle conductors with the combination of high-speed printing and high-speed sintering for low-cost electronics manufacturing.

Keywords: Printed electronics, metal nanoparticle sintering, process monitoring, frequency-domain thermoreflectance (FDTR), inkjet printing, intense pulsed light (IPL) sintering

1 Introduction

The next age of electronic devices and systems will be centered on personalized diagnostic, wearable human-interactive devices, and the internet of things. Printed electronics ushers in this age with the benefits of large-area, low-cost, rapid manufacturing, and compatibility with flexible substrates such as plastic and paper.[1,2] Printing technology has been used to fabricate various microelectronic devices, including semiconductor devices such as transistors [3] and organic solar cells [4], or thermal devices such as heaters [5], thermoelectric energy harvesters [6] and temperature sensors [7]. There are different options of metallic inks and pastes to print metal traces for these devices. Metal nanoparticle (MNP) ink is one of the prominent candidates for fabricating conductive traces due to its high solute mass loading and flexibility to adjust rheological parameters for different printing methods. Often, binders and surfactants are used in these inks to suspend the metallic content, e.g., nanoparticles/wires [8,9] in a solution. Chemistries are optimized to achieve prolonged shelf-life, the desired printed morphology, and a low post-processing temperature. However, these additives hinder electronic conduction between the metal particles in the as-printed state. Therefore, the as-deposited liquid ink needs to undergo a sintering process at an elevated temperature to become electrically conductive.

Traditional thermal baking as a means of sintering is problematic for several reasons. Incompatibility with the thermal stability of commonly used low-cost polymer substrates is the primary reason.[10,11] Secondly, the slow sintering dynamics of this method renders it ineffective in a roll-to-roll, rapid manufacturing production environment. Intense pulsed light (IPL) sintering is a more promising method in these regards as heat is generated by brief millisecond pulses from a high-intensity flash lamp. The light is only absorbed by the metal nanoparticle pattern but not by the plastic substrate. The targeted irradiation means the metal cools down fast when the illumination has ceased, limiting the temperature rise of the underlying plastic substrate and averting damage to the substrate.[12] Additionally, this ultrafast technique reduces the post-fabrication thermal processing time to a few seconds, therefore, increasing manufacturing throughput.[13]

During process development and manufacturing, monitoring of the sintering process to control the quality of the sintered metal ink is crucial. Researchers have developed different measurement modalities to monitor the changes that take place during sintering, such as a change in structural/surface morphology, optical properties, or transport phenomena. These measurement methods can be classified into two categories: contact and non-contact methods. One easy and obvious contact method is to measure electrical conductivity to investigate different stages of sintering.[14,15] This has the advantage of directly measuring the property that is most important for most printed metal nanoparticle applications. However, it requires dedicated contacts to be fabricated or probes that can scratch the material and takes time to align. Dilatometry is another contact method that determines length or volume as a function of temperature. During the sintering process, dilatometry can sense only one-dimensional length changes because of shrinkage (thickness in the case of thin films). Typically, the length scale of printed metallic traces would be too small for this method, requiring that the material be appropriately prepared for quantification.[16] Overall, contact methods suffer from their destructive nature and difficult setup for an automated production line.

Non-contact evaluation of the sintering process is gaining interest because of its ability to keep the test material intact while monitoring the sintering steps. Additionally, it has the potential for in-line and real-time monitoring. There are numerous non-contact methods for sintering process evaluation for metal additive manufacturing (AM), especially in powder metallurgy. These methods include ultrasonic/acoustic measurement, optical tomography, electromagnetic, and eddy current techniques.[17] Generally, these methods are employed for in-line detection of defects and porosity during/after the sintering. None of these techniques have been applied in the field of printed electronics, which uses different material chemistries, different substrates, smaller particle sizes, thinner films, and smaller feature sizes than powder metallurgy. Recently, millimeter wave imaging and terahertz (THz) time-domain spectroscopy (TDS) have been used for non-contact characterization in printed electronics utilizing the non-destructive nature of THz radiation. THz imaging has been used to characterize printed ink based on black carbon.[18] This approach was not compatible with high-yield production lines because of its time-consuming nature and complicated data processing for effective extraction of conductive properties. A simpler and faster method of characterizing with THz TDS was developed by Zhuldybina et al. exploiting the distinctive THz range signal generated by printed V-shaped antennas.[19] Although this is a facile characterization method by monitoring these antennas' transmission, it needs an extra antenna pattern to be printed side by side with the actual features of interest. Zenou et al. monitored the changes in spectral reflectivity of a metal nanoparticle ink during sintering as a possible non-contact method.[20] However, this method can only qualitatively differentiate between the sintered and the non-sintered state. The changes in reflectance between both states are so abrupt that the reflectivity versus resistivity graph could not discern any gradual changes from the non-sintered state to the sintered state. Another optical technique was demonstrated by Cherrington et al. using colorimetry but suffers from scatter in the data.[21] Abbel et al. have demonstrated a method where an embedded temperature probe is used to monitor the temperature rise in a metallic ink during flash sintering.[22] Examining the temperature rise as well as the duration of the temperature exposure, one can indirectly monitor the process; however, this does not generate direct information of the desired changes in material properties during sintering.

Here, we apply an optical pump-probe technique known as frequency-domain thermoreflectance (FDTR) to monitor the sintering of inkjet-printed and flash-sintered conductive features. This method uses thermal conductivity as the measurement modality. Thermal conductivity is an important material property in its own right, for example, for thermal devices. Additionally, it can be directly converted into electrical conductivity using the Wiedemann-Franz Law for metals. Therefore, FDTR is a rapid non-contact measurement method that directly probes changes in the material during nanoparticle sintering.

FDTR measures the thermal lag between the pump and the probe laser through the thermoreflective property of materials - the relative change in surface reflectivity as a function of temperature.[23] A frequency-modulated pump laser periodically heats up the sample's surface. This periodic heat flux, caused by the sample's absorption of the pump light, oscillates the temperature at the sample's surface. The unmodulated probe laser, which is reflected from the sample, is used to measure sample reflectivity and hence the temperature response. A lock-in amplifier, locked at the pump frequency, measures its phase. The phase data is used to extract the thermal properties of the sample by fitting the solution of the thermal diffusion equation.[24]

Recently, we have shown that FDTR can be used to measure the thermal conductivity of a silver nanoparticle film fabricated by spin coating and thermal sintering on a hotplate.[25] Here, this method is expanded to methods compatible with high-throughput manufacturing, namely inkjet printing and rapid IPL sintering with FDTR characterization. Inkjet printing is a scalable technique for printed electronics. Designs can be customized on-the-fly as inkjet printing is drop-on-demand where drops are ejected from a nozzle when a voltage pulse is applied to a piezoelectric actuator. The substrate is translated relative to the nozzle and drops coalesce on the substrate to form the final pattern. See Figure 1 for an illustration of the envisioned in-line monitoring in a high-throughput manufacturing line. Initially, we demonstrate the compatibility of these different fabrication methods with FDTR using a full frequency sweep. The extracted in-plane thermal conductivity agrees well with other measures of sintering, namely electrical conductivity, and surface morphology. This measurement was used as a baseline measurement. However, a full frequency sweep takes around six and a half minutes in total, which is not desirable to be used in high-throughput manufacturing.

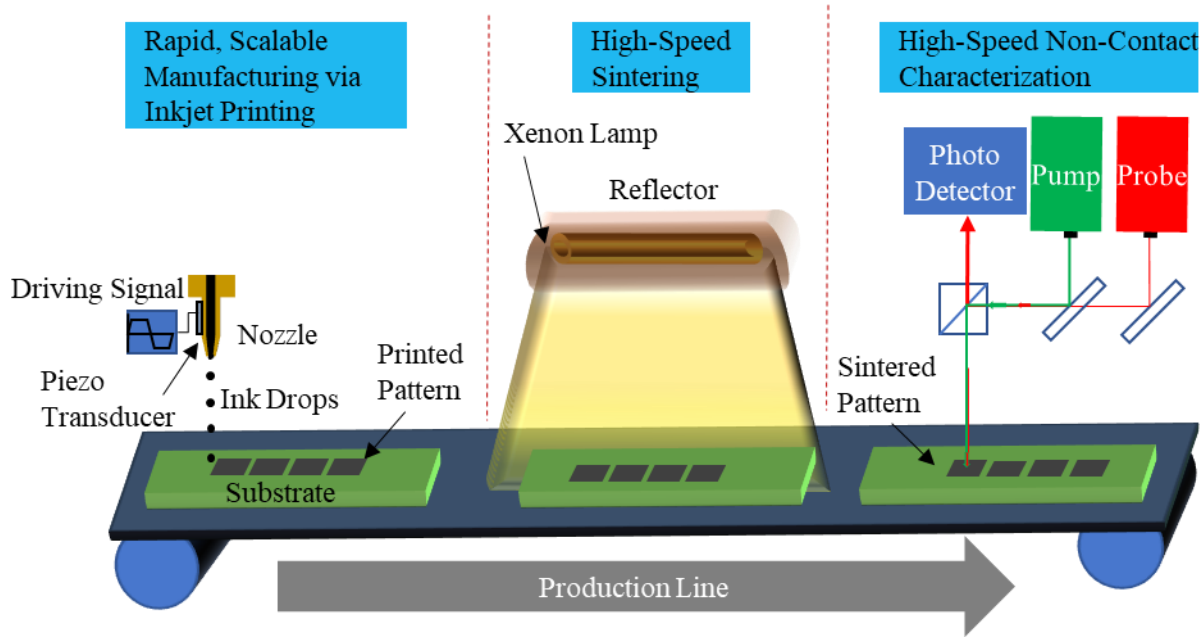

Figure 1. Illustration of a potential roll-to-roll production line. First, metal nanoparticle features are deposited and patterned with a scalable and fast fabrication method: drop-on-demand inkjet printing. A voltage waveform drives the piezo actuator, connected to the nozzle, to eject ink droplets. Movement of the substrate relative to the nozzle creates the pattern of droplets on the substrate. In the second step, a Xenon lamp provides ultrafast flash light sintering using the photothermal effect. In the third step, a non-contact, optical pump-probe measurement characterizes the sintered features in terms of thermal conductivity. This value can be used to make decisions on the quality of sintering.

This is overcome by selecting a subset of six frequencies to perform the measurement on. This reduces measurement time without significantly sacrificing goodness of fit of the thermal model to the measured data. Additionally, these six frequency data points can be measured simultaneously by including all frequency components in the pump amplitude modulation, and demodulating all frequencies concurrently. By implementing these two strategies together, the measurement could be performed in 12 seconds while increasing uncertainty relative to the baseline by 5%. This increases the compatibility of this method with a high-throughput manufacturing environment. Finally, a Monte Carlo Simulation was performed to predict limitations on further improvements in measurement time by the contribution of added phase noise. This simulates the effect of lower integration time of the lock-in amplifier, which would result in much faster measurement but also increases phase noise. This estimates the propagation of introduced random noise to the properties derived from the analysis of FDTR data.[26] It is shown that the measurement time can be cut down to hundreds of milliseconds and still be within 3.5% of the baseline value.

2 Materials and Methods

2.1 Fabrication by Inkjet Printing

Nanoparticle films are fabricated on glass using a commercial silver nanoparticle ink (ANP DGP 40LT-15C, Advanced Nano–Products, Co., Sejong, Korea). The nanoparticle diameter is 35 nm, suspended in the major solvent Triethylene Glycol Monoethyl Ether (TGME). A custom-built inkjet printer with a nozzle of 60 µm diameter (MJ-ATP-01-60-8MX, Microfab Technologies, Inc., Plano, TX) is used to jet and deposit square patterns. The ink's viscosity is in the range of 15-17 mPa.s and a trapezoidal bipolar waveform of 56 V peak-to-peak was applied to the nozzle's piezoelectric actuator to achieve stable jetting. The printer follows an inward spiral filling to fabricate the square patterns (area ~1 mm^2) with a drop spacing of 120 µm.

2.2 Post-Processing by Intense Pulsed Light Sintering

The prepared films are subjected to a drying step at a temperature of 50°C for 2 hours before performing intense pulsed light sintering (X-1100, XENON Corporation, Wilmington, MA). We sintered dried films with different IPL parameters to monitor the progression of electrical conductivity with these parameters. All sintering steps are done at room temperature and under ambient conditions. We control the pulse fluence (energy density, J/cm^2 per pulse) by changing the capacitor bank voltage driving the Xenon lamp while keeping the pulse width constant (4.5 ms). Various values of pulse fluence are used ranging from zero to 7.3 J/cm^2 to monitor their effect on electrical conductivity. The effect of pulse count is also studied at fixed pulse fluence and pulse width. For all IPL sintering experiments, the samples were placed ~1 inch away from the lamp surface.

2.3 Characterization by Frequency-Domain Thermoreflectance

The details of the setup for thermal conductivity measurement using FDTR are shown in Figure 2. The setup is based on two continuous-wave lasers operating at wavelengths of 515 nm (pump) and 785 nm (probe). The pump laser is intensity modulated at different frequencies with an analog signal and passes through a 40X objective to be focused onto the sample's surface. The $1/e^2$ radius

of the laser spot on the sample is approximately 1.25 μm. The probe laser stays unmodulated. Both of the lasers pass through optical isolators to prevent the beams from reflecting back, avoiding destabilization of the lasers. Half-wave plates, a polarizing beam splitter (PBS), and a quarter-wave plate (QWP) are used to maximize the amount of light reaching the sample and then back towards the detector. Typically, a transducer layer, an extra metallic layer, is deposited onto the surface of samples, which acts as both thermometer and heater. However, owing to the strong thermoreflectance coefficient of silver at the probe wavelength, no transducer layer was needed on top of the printed samples. On the surface of the sample, the absorbed modulated pump signal causes a periodic heat flux at the modulation frequency and an additional thermal phase $\theta_{thermal}$. The probe laser samples this temperature response and is measured by a photodetector and a lock-in amplifier with the same modulation frequency. Like other FDTR measurements, two measurements are carried out to isolate this thermal phase from other experimental contributions to the phase signal. The first measurement, referred to as the thermal measurement, is performed via measuring the phase of the probe beam ($\theta_1=\theta_{thermal}+\theta_{optical}+\theta_{electrical}+\theta_{reference}$, where the additional phase components are unwanted but contribute to the signal). The second measurement is known as the reference measurement measuring just the pump beam ($\theta_2=\theta_{optical}+\theta_{electrical}+\theta_{reference}$). Since both beams travel the same distance electrically and optically, $\theta_{thermal} = \theta_1 - \theta_2$. The pump power in the reference measurement is set to match the probe power during the thermal measurement. At these powers, we observe no dependence of the phase signal on the power of the lasers. The measured thermal phase is fit to a model based on the Fourier Law to obtain the thermal conductivity of the thin film.[27] To avoid any laser sintering by the pump beam and changes to the sample's properties, the laser power is kept small (~100 μW). The root-mean-square (RMS) surface roughness is about 10 nm for this metallic nanoparticle ink (see Figure S1). For the 1.25 μm spot size, the roughness is insignificant to distort the reflected signal. For significant (micron-sized) topographical changes or any pores on the surface of the sample, a live optical image feed was used to look at the surface and avoid micron-sized pores or non-idealities on the surface. However, more generally, the FDTR technique relies on the phase difference between the pump and the probe laser, not signal amplitude. As long as reflectance is large enough to obtain a sufficiently large signal, the result does not depend directly on the value of reflectance. Therefore, any change in reflectance due to the nanometer scale surface roughness does not impact the measurement result.

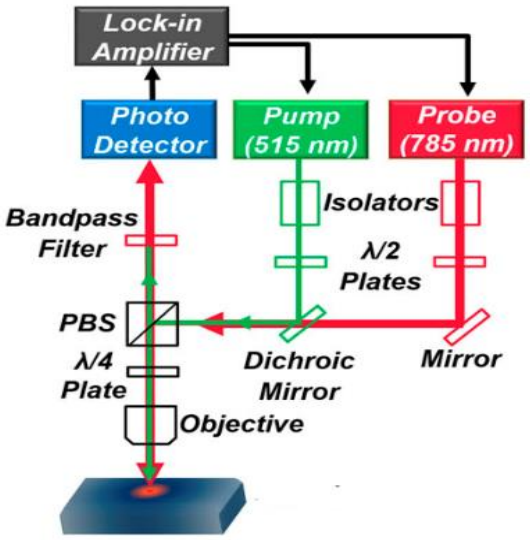

Figure 2. Schematic of the FDTR setup; a pump laser periodically generates a heat flux in a spot on the sample surface. The probe laser is reflected from the same spot with an additional thermal phase. A lock-in amplifier measures the phase lag between the reflected pump and probe lasers. The laser beams are guided via the mirrors and objectives. A bandpass filter collects only the probe signal and the photodetector converts it to an electrical signal

2.4 Baseline Characterization

To compare with FDTR results, the Van der Pauw method was used to measure electrical sheet resistance with a Semiconductor Parameter Analyzer (Keithley 4200A-SCS, Tektronix, Beaverton, OR). The sheet resistance is converted to resistivity from the film thickness measured with a stylus profilometer (Alpha-Step, D-600, KLA-Tencor, Milpitas, CA). We used equation (1) for calculating electrical resistivity. Here, R_s and t are the sheet resistance and film thickness.

$$\rho = R_s * t \quad (1)$$

$$k = \sigma * L * T = \frac{L*T}{\rho} \quad (2)$$

Thermal conductivity is calculated from measured electrical conductivity with the Wiedemann-Franz Law, equation (2), where k is thermal conductivity, σ is electrical conductivity from sheet resistance, T is room temperature, and L is the Lorentz number, which is $2.37*10^{-8}$ $W\Omega/K^2$ for silver. A Field Emission Gun Scanning Electron Microscope (FEG-SEM, Fisher Quanta 3D) is used for capturing the surface morphology of the films at different stages of sintering.

3 Results and Discussion

Well-defined squares with minimal corner-rounding are printed with negligible coffee ring effect, ensuring the uniformity of the material deposition. Figure 3 (a) shows typical jetting stability. Figure 3 (b) shows the shape of printed squares on the glass. The thickness of these squares is 650 ±120 nm. A typical thickness profile is shown in Figure 3 (c). The thickness variation in a single rectangle is within 10% of its average value. This uncertainty in thickness is sufficiently small to

reliably extract thermal properties from FDTR results where thickness is a parameter in the analytical FDTR model.

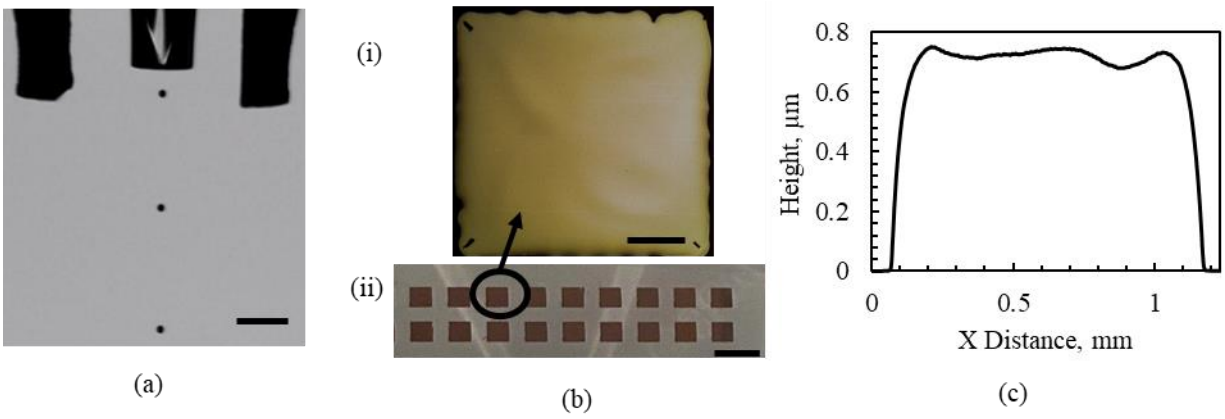

Figure 3. (a) Stroboscopic image of stable jetting with a bi-polar trapezoidal waveform provided to the piezo-actuator of the nozzle. Scale bar represents 500 µm. (b) (i) Zoomed in optical micrograph of one of the squares, the scale bar represents 250 µm (ii) An array of printed squares, the scale bar represents 2 mm. c) A representative example of a height profile of a printed square.

The electrical conductivity increases as the pulse fluence, i.e., energy density per pulse, is increased as shown in Figure 4 (a). Here, the number of pulses is fixed to 30 so that the effect of pulse fluence on electrical conduction can be observed. From 2.8 J/cm^2 to 5.91 J/cm^2, the electrical conductivity increases sharply from $5.47*10^6$ to $1.99*10^7$ S/m. At 7.26 J/cm^2, there is a decline in electrical conductivity due to over-sintering, later confirmed through SEM images. Figure 4 (b) represents the effect of the number of pulses as well as total energy density on the electrical conductivity. In this case, the pulse fluence was kept constant at 5.91 J/cm^2. Total energy density is calculated by multiplying the pulse number with the pulse fluence. The highest electrical conductivity, $2.26*10^7$ S/m, is found when the sample is subjected to 45 pulses. This value is 35% of the bulk silver conductivity, matching our previous results using thermal sintering.[25]

The measured phase signal's sensitivity in response to the in- and out-of-plane thermal conductivity (k_r and k_z respectively) is shown in Figure 5 (a). We fit for both parameters in the thermal model. From the sensitivity plot, one can see that the phase sensitivity for k_r is larger than for k_z. Generally, we obtain k_z values that are larger than k_r and close to bulk silver pointing to an anisotropy in the film. However, due to the low sensitivity to k_z, the outcome of the fit for k_r, the desired output of these experiments, does not depend significantly on whether k_z is a fitting parameter or assumed constant at the bulk silver value. Within the frequency range considered, a higher modulation frequency results in a higher sensitivity. However, at higher frequencies the measurement noise increases too. Therefore, the measurement is limited up to 10 MHz. The results are somewhat sensitive to all other thermophysical parameters of the system as inputs to the fit such as optical spot size, volumetric heat capacities of the film and the substrate, thermal conductivity of the substrate, and thickness of the substrate and film (see Figure S2 for sensitivity

plot and Figure S3 for effect on uncertainty). Notably, the sensitivities (except for the spot size) are much lower than the sensitivity to the in-plane thermal conductivity of the silver film. Additionally, in a manufacturing setting, they should be assumed to be constant and known beforehand. A typical experimental phase vs modulation frequency plot with the analytical fit for a silver nanoparticle/glass sample is shown in Figure 5 (b). This represents the goodness of the fit between the measured and fitted values. Figure 5 (c) shows the in-plane thermal conductivity from FDTR measurements and thermal conductivity calculated from electrical conductivity using the Wiedemann-Franz Law with respect to pulse fluence. For both measurements, thermal conductivity shows the highest value, 144.65 W/m.K at around 5.91 J/cm^2 and decays down at 7.3 J/cm^2. Figure 5 (d) shows the thermal conductivity from FTDR and converted from Wiedemann-Franz Law with pulse count as well as total energy density. Again, electrical measurements and FDTR agree well.

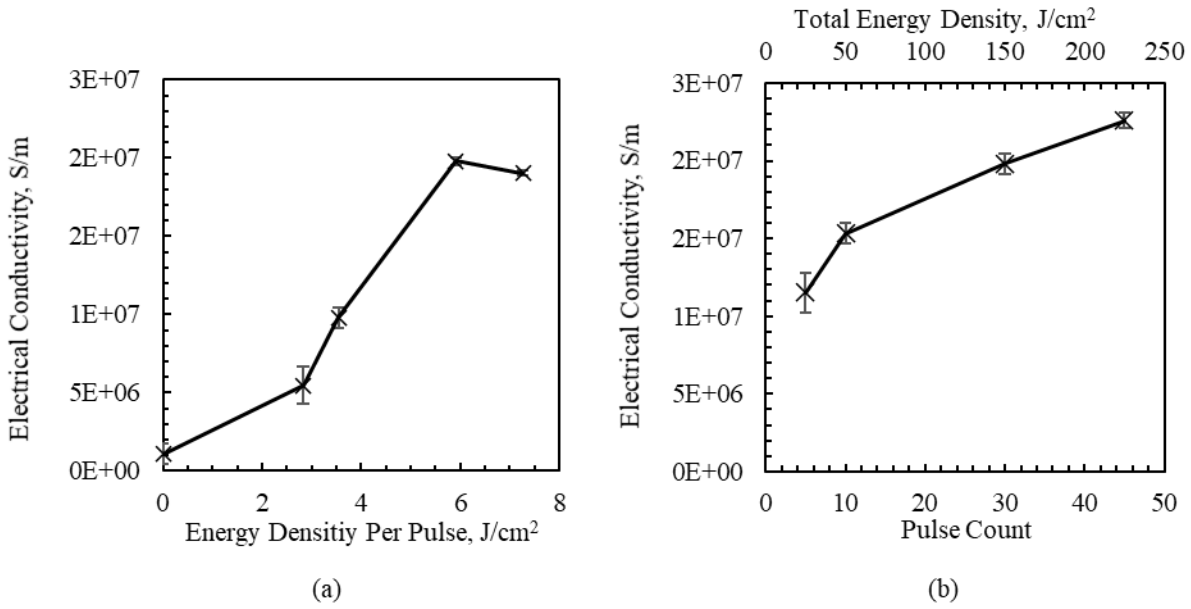

Figure 4. (a) Change in electrical conductivity as a function of pulse fluence. Films become more conductive with increasing fluence until over-sintering occurs. Pulse count was kept constant at 30. (b) Electrical conductivity after IPL sintering increases with increasing pulse count with the same pulse fluence (5.91 J/cm^2). The secondary axis shows the total energy density with increasing pulse count.

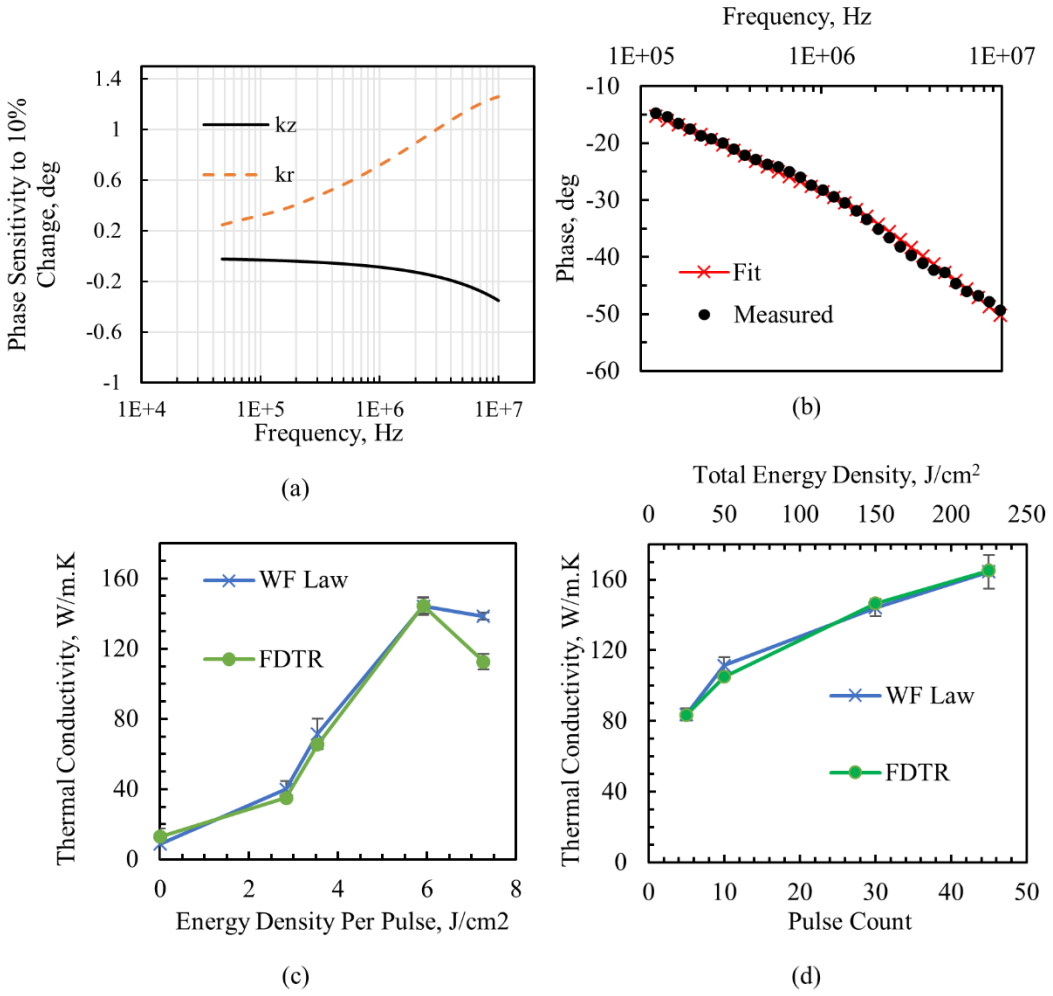

Figure 5. (a) The sensitivity of the measured thermal phase to the in-plane and out of plane thermal conductivity. (b) A representative example of the thermal phase vs. frequency plot of measured FDTR data and fitted through analytical modeling, representing a good agreement between fit and measured data. (c) Thermal conductivity after IPL sintering at different values of pulse fluence measured using FDTR and calculated from electrical conductivity using Wiedemann-Franz Law. (d) Effect of pulse count on thermal conductivity from FDTR and Wiedemann-Franz Law. The highest thermal conductivity is found at 45 pulses.

Figure 6 shows the surface morphology SEM images of films for different values of pulse fluence. Figure 6 (a) shows a representative example of an under-sintered case. The individual grains are visible with less contact with neighboring nanoparticles. In the well-sintered case (Figure 6 (b)), the grain shapes are not spherical, and long necks have grown. A noticeable percolation network for carrier transport is established; hence, the highest thermal conductivity is found. However, with a high fluence such as 7.3 J/cm^2, both the number and the size of pores increase due to excessive sintering (Figure 6 (c)). The effect of such over-sintering is evident in the declining thermal and electrical conductivity values. The increasing pore size can also affect the film's heat capacity, which is a parameter of the thermal model. We fit the thermal model for

heat capacity and in-plane thermal conductivity for an over-sintered film, which is highly porous and therefore the worst case. With an excellent fit, volumetric heat capacity was found to be $2.35*10^6$ J/m^3.K, which is close to the otherwise assumed bulk value for silver of $2.5*10^6$ J/m^3.K, and thermal conductivity decreased by about 4%.

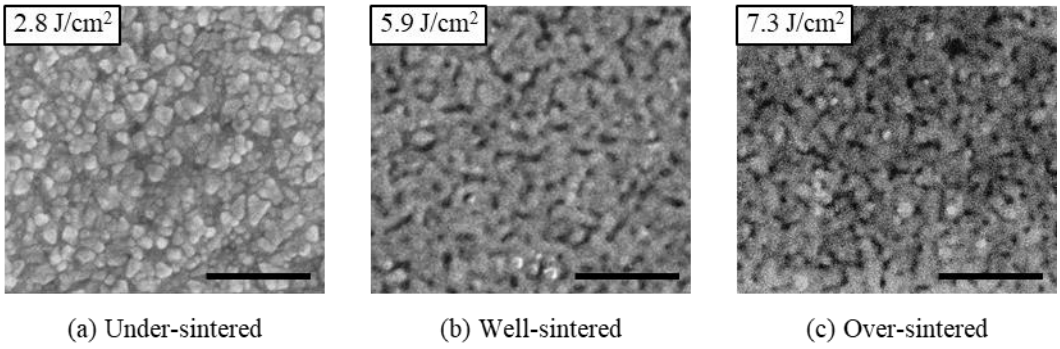

Figure 6. SEM images of the surface morphology for different sintering conditions with different values of pulse fluence and the same pulse count (30). Scale bar represents 500 nm. (a) Individual grains are visible as the sample was under-sintered at low pulse fluence (2.8 J/cm^2). (b) Well-sintered samples with a moderate pulse fluence (5.9 J/cm^2), exhibiting a well-defined percolation network. (c) Slightly over-sintered case with increased number of pores with increased pore size at high pulse fluence (7.3 J/cm^2).

Next, we performed an experiment where fewer frequency-vs-phase data points are taken and the same analytical model was fitted to this measured data. The rationale behind this experiment is that the fewer data points are experimentally measured, the lower the time for each measurement will be. Unlike the previous measurement, where each measurement serially captured 32 frequency-vs-phase data points, only six points are taken now. Moreover, a multi-frequency lock-in amplifier (Zurich Instruments HF2LI) simultaneously modulates the pump signal with these six frequencies, and hence all the points are measured at the same time. In this way, the characterization time was lowered to 12 seconds, whereas the full frequency sweep would take more than six minutes. Figure 7 (a) shows that the computed data from the diffusive thermal model fits these six measured frequency data points well. Figure S4 shows the measurement uncertainty determined from a Monte Carlo simulation with a phase error of 1 degree for different numbers of frequency data points. With a decreased number of frequency points (which are the number of modulator/demodulator modules running at once), the uncertainty in measuring thermal conductivity in three differently sintered materials tends to increase. From thirty-two to six frequency data points the uncertainty only increases from about 2% to about 5%. Below six frequencies, which is the maximum number in our system, the uncertainty increases further and there exists a trade-off between measurement uncertainty and number of modulators. Figure 7 (b) shows the comparison of two experiments with respect to their phase values. The two experiments were taken on different spots on the same sample, one with the full frequency sweep and one with only six data points. A small discrepancy can be observed but the fitted in-plane thermal

conductivity agreed within 5% (87.66 W/m.K for six-point measurement, 83.85 W/m.K for full modulation frequency sweep). This attests to the viability of using just six frequencies as well as the repeatability of the inkjet printing and IPL sintering processes. The remaining discrepancy between the measurements can generally be attributed to spatial variability of the samples and increased measurement uncertainty with fewer frequency data points (see Figure S4). In short, by sacrificing a small amount of accuracy in the measured thermal conductivity, the whole characterization time can be cut down to seconds.

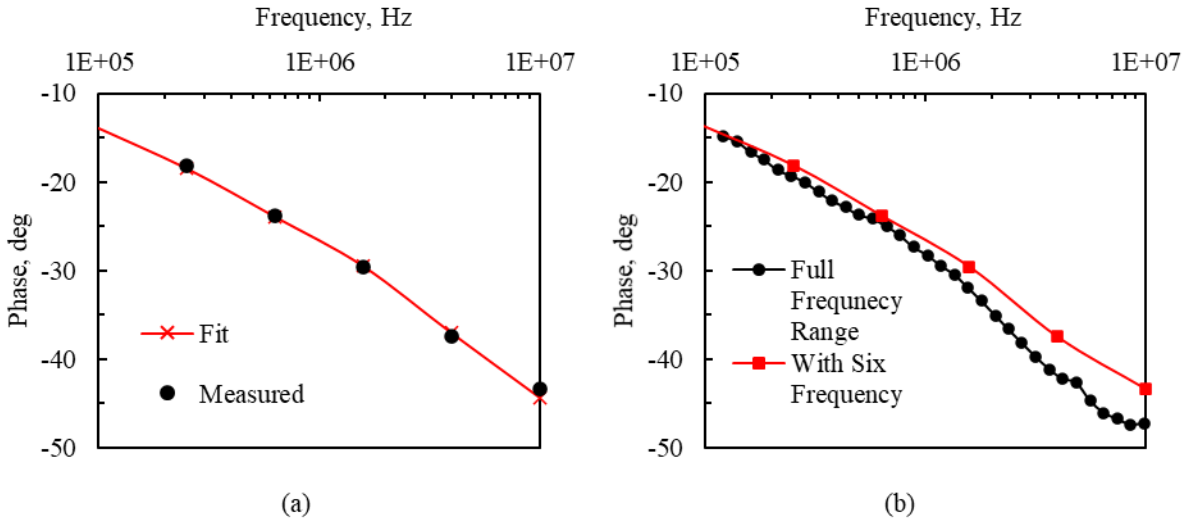

Figure 7. (a) Comparison of the thermal phase data from the measurement and the analytical fit. The solid line represents the analytical solution with the diffusive thermal modeling that fits the measured values well. (b) Comparison of the phase data between two experiments on different sample locations, one is with the full frequency range, which takes longer than the other having only six frequencies measured simultaneously.

4 Prediction of Faster Measurement

A lock-in amplifier always poses a trade-off between improved accuracy with longer integration time versus a faster measurement. The integration time corresponds to the inverse of the bandwidth of the low-pass filter in the lock-in amplifier, which is used to exclude higher frequency components of the signal such as noise. The lower the integration time, the shorter the lock-in amplifier takes to complete the measurement. The total experimental measurement time of 12 s uses an effective integration time of 3 s (averaging over 10 measurements each with integration time 0.3 s). Before taking the measurement, we wait another 3 s for the measurement to settle. This 6 s procedure is repeated to make a reference measurement to null the other unwanted phase contributions. This is a conservative approach and the measurement time can likely be reduced by reducing the time to wait for the measurement to settle as well as the time for the reference measurement, which has a larger signal to noise ratio than the actual measurement. In addition to the actual measurement time, changing from the thermal to the reference measurement requires changing a bandpass filter before the detector. Currently we do this manually requiring a few

seconds, but this could be done automatically in less than a second. However, the most direct approach to reduce measurement time is by reducing the integration time, but this also results in noisier data. Therefore, the extracted thermal conductivity from such data will be more uncertain.

Here, a Monte Carlo computational approach is employed to calculate the measurement uncertainty by introducing phase noise to existing FDTR data and observing the trend of the deterioration in the fitted thermal conductivity values with increased noise. The more noise we can afford within an acceptable tolerance level, the shorter the integration time we can use, and the faster the measurement becomes. A static phase measurement at different modulation frequencies for different lock-in integration times was conducted. The measurement shows that the distribution of phase noise values is mainly a normal distribution. We used these values to determine the phase noise at different frequencies and integration times. Figure 8 (a) shows this experiment's results with four different frequencies ranging from 160 kHz to 10 MHz. From the sensitivity plot in Figure 5 (a), it can be concluded that the highest sensitivity is at higher frequencies, but these data points tend to also be noisier than low frequencies. The phase noise dependence on frequency was modeled by fitting a power law of the form $y=a*x^b$ for each of the three studied integration times. This model is used to predict the effect of phase noise on thermal conductivity measurements with different integration times. The noise is significantly reduced when integration time is increased from 0.02 s to 0.3 s. However, beyond 0.3 s other noise sources dominate that cannot be removed by averaging on this timescale, such as laser phase instability. Therefore, the phase noise vs frequency characteristics are very similar for 0.3 s and 2 s integration time. Three different samples with three different thermal conductivities are taken, and frequency-dependent random noise for different integration times is added to their respective experimental phase values. Figure 8 (b-c) represents such an example. In Figure 8 (b), the analytical model is fit to the phase data obtained from a typical full frequency sweep. Figure 8 (c) represents such a fit to the same dataset with an addition of frequency-dependent random phase noise for 0.3 s integration time. Such cases of random noise addition and fitting to the data were done for 100 independent iterations to provide statistical significance. The statistical variation of the extracted thermal conductivity values represents to what extent the noise affects the deduced thermal conductivity. Figure 8 (d) shows a representative histogram of 100 fits for samples with high thermal conductivity. The standard deviation of this histogram represents the uncertainty of extracted thermal conductivity associated with the phase noise, compared to the baseline measurement where 32 points are used to fit the FDTR curve. The same procedure is applied for three different samples with a low, mid, and high value of thermal conductivity. Figure 8 (e-f) shows a summary of the complete analysis. Figure 8 (e) represents the uncertainty in thermal conductivity values with a full set of 32 data points with added noise as a function of integration time. Here, adding these noise values would typically cause a 2.1% variation with respect to the baseline FDTR measurement for 2 s and 0.3 s integration time, which exhibit very similar noise. For 0.02 s, the uncertainty increases to about 10.5% on average. Since the largest noise occurs for high frequencies, this can be somewhat mitigated by limiting the frequency range to 3 MHz (24 frequency data points) reducing uncertainty to 9.3% for 0.02 s integration time. Figure 8 (f) shows the same graph using only six logarithmically spaced points of the FDTR curve. It is noted that these six points can be measured simultaneously. This added noise causes uncertainty of 5.7% with respect to the baseline FTDR measurement for 2 s

and 0.3 s integration time. For 0.02 s, the uncertainty increases to about 27.9% on average. Again, this can be reduced to 19.9% by limiting the maximum frequency to 3 MHz using six logarithmically spaced frequencies, but this level of uncertainty may still not be acceptable depending on the application. However, measurements can be made in one shot over six frequencies with an integration time of 300 ms. This would ideally cut down the measurement time to be some hundreds of milliseconds, and the extracted value would be within 3.5% of the baseline measurement by limiting the maximum frequency to 3 MHz. This minimization of measurement time could be acceptable for process monitoring on an industrial scale.

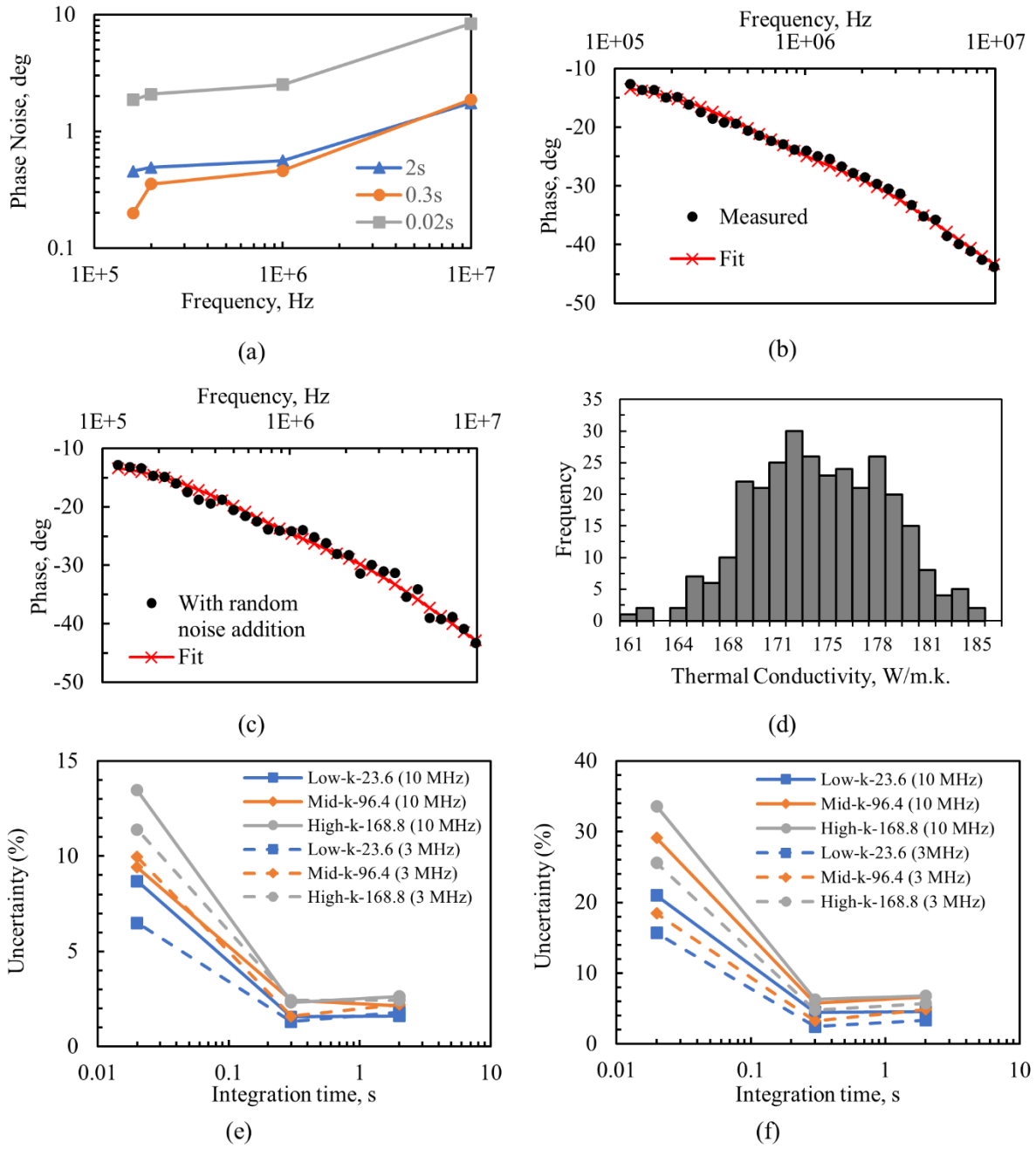

Figure 8. (a) Standard deviation (noise) of static measurements of phase at different modulation frequencies for different lock-in integration times. (b) Analytical model fits to the measured data of a sample with high thermal conductivity. This used 32 frequency points, which is considered as the baseline measurement. (c) Frequency-dependent phase noise for 0.3 s integration time is added randomly to the same phase data and is fitted using the same thermal model. (d) Histogram of 300 fits for high thermal conductivity samples and 0.3 s integration time; mean and standard deviation of this distribution indicate the conductivity variations as a result of these noise addition. (e) Calculation of uncertainty of the thermal conductivity using all 32 points of the FDTR curve while adding frequency-dependent noise values up to 10 MHz and 24 points up to 3 MHz. (f) Same

calculation of uncertainty using only six frequency points that are logarithmically spaced on the FTDR curve up to 10 MHz and 3 MHz.

5 Conclusion

To conclude, a novel, non-contact characterization and process monitoring technique is demonstrated for printed electronics based on thermoreflectance. Different stages of intense pulsed light sintering of inkjet-printed metal nanoparticle patterns can be distinguished. The method measures thermal conductivity, which can be used to quantify electrical conductivity. Furthermore, the compatibility of this method with high-throughput production is shown by reducing measurement time to 12 seconds using only six frequency data points that are measured simultaneously. Future quantitative study could determine the spatial variability within printed rectangles. A predictive model based on Monte Carlo simulation is proposed to cut down the measurement time even further to hundreds of milliseconds with an acceptable error in measurement of 3.5% by reducing the integration time of the lock-in amplifier. Future experimental work using a smaller integration time combined with a small number of frequency data points could be undertaken to confirm the prediction.

Acknowledgements

We acknowledge the support of the Natural Sciences and Engineering Research Council of Canada (NSERC), funding reference number STPGP 521480-18. SEM images were obtained at the Advanced Light and Electron Microscopy Facility at York University.

References

[1] Arias A C, MacKenzie J D, McCulloch I, Rivnay J and Salleo A 2010 Materials and applications for large area electronics: Solution-based approaches *Chemical Reviews*

[2] Grau G, Kitsomboonloha R, Swisher S L, Kang H and Subramanian V 2014 Printed transistors on paper: Towards smart consumer product packaging *Advanced Functional Materials*

[3] Kang B, Lee W H and Cho K 2013 Recent advances in organic transistor printing processes *ACS Applied Materials and Interfaces*

[4] Lipomi D J, Tee B C-K, Vosgueritchian M and Bao Z 2011 Stretchable Organic Solar Cells *Advanced Materials* **23** 1771–5

[5] Zeng P, Tian B, Tian Q, Yao W, Li M, Wang H, Feng Y, Liu L and Wu W 2019 Screen-Printed, Low-Cost, and Patterned Flexible Heater Based on Ag Fractal Dendrites for Human Wearable Application *Advanced Materials Technologies* **4** 1800453

[6] Varghese T, Hollar C, Richardson J, Kempf N, Han C, Gamarachchi P, Estrada D, Mehta R J and Zhang Y 2016 High-performance and flexible thermoelectric films by screen printing solution-processed nanoplate crystals *Scientific Reports* **6** 33135

[7] Aliane A, Fischer V, Galliari M, Tournon L, Gwoziecki R, Serbutoviez C, Chartier I and Coppard R 2014 Enhanced printed temperature sensors on flexible substrate *Microelectronics Journal*

[8] Volkman S K, Yin S, Bakhishev T, Puntambekar K, Subramanian V and Toney M F 2011 Mechanistic Studies on Sintering of Silver Nanoparticles - Chemistry of Materials (ACS Publications)

[9] Sun Y, Gates B, Mayers B and Xia Y 2002 Crystalline Silver Nanowires by Soft Solution Processing *Nano Letters*

[10] Schroder K A, McCool S C and Furlan W F 2006 Broadcast photonic curing of metallic nanopartiele films *Technical Proceedings of the 2006 NSTI Nanotechnology Conference and Trade Show* **3** 198–201

[11] Schroder K A 2011 Mechanisms of photonic curingTM: Processing high temperature films on low temperature substrates *Nanotechnology 2011: Electronics, Devices, Fabrication, MEMS, Fluidics and Computational* **2** 220–3

[12] Wünscher S, Abbel R, Perelaer J and Schubert U S 2014 Progress of alternative sintering approaches of inkjet-printed metal inks and their application for manufacturing of flexible electronic devices *Journal of Materials Chemistry C* **2** 10232–61

[13] Jang Y R, Joo S J, Chu J H, Uhm H J, Park J W, Ryu C H, Yu M H and Kim H S 2020 A Review on Intense Pulsed Light Sintering Technologies for Conductive Electrodes in Printed Electronics *International Journal of Precision Engineering and Manufacturing - Green Technology* 1–37

[14] Jang Y R, Ryu C H, Hwang Y T and Kim H S 2020 Optimization of Intense Pulsed Light Sintering Considering Dimensions of Printed Cu Nano/Micro-paste Patterns for Printed Electronics *International Journal of Precision Engineering and Manufacturing - Green Technology* 1–15

[15] Hwang H-J, Chung W-H and Kim H-S 2012 *In situ* monitoring of flash-light sintering of copper nanoparticle ink for printed electronics *Nanotechnology* **23** 485205

[16] German R M 1996 *Sintering theory and practice* (New York: Wiley)

[17] Taheri H 2018 Nondestructive evaluation and in-situ monitoring for metal additive manufacturing *Graduate Theses and Dissertations*

[18] Zeng Y, Edwards M, Stevens R, Bowen J J, Donnan R S and Yang B 2017 Terahertz characterisation of UV offset lithographically printed electronic-ink *Organic Electronics* **48** 382–8

[19] Zhuldybina M, Ropagnol X, Trudeau C, Bolduc M, Zednik R and Blanchard F 2019 Contactless In Situ Electrical Characterization Method of Printed Electronic Devices with Terahertz Spectroscopy *Sensors* **19** 444

[20] Zenou M, Ermak O, Saar A and Kotler Z 2014 Laser sintering of copper nanoparticles *Journal of Physics D: Applied Physics* **47** 025501

[21] Cherrington M, Claypole T C, Gethin D T, Worsley D A and Deganello D 2012 Non-contact assessment of electrical performance for rapidly sintered nanoparticle silver coatings through colorimetry *Thin Solid Films* **522** 412–4

[22] Abbel R, Van Lammeren T, Hendriks R, Ploegmakers J, Rubingh E J, Meinders E R, Groen W A and Groen W A 2012 Photonic flash sintering of silver nanoparticle inks: A fast and convenient method for the preparation of highly conductive structures on foil *MRS Communications* **2** 145–50

[23] Schmidt A J, Cheaito R and Chiesa M 2009 A frequency-domain thermoreflectance method for the characterization of thermal properties *Review of Scientific Instruments* **80** 094901

[24] Feser J P and Cahill D G 2012 Probing anisotropic heat transport using time-domain thermoreflectance with offset laser spots *Review of Scientific Instruments*

[25] Rahman M S, Rahman M, Pisana S and Grau G 2019 Effect of sintering conditions on the thermal properties of printable metal nanoparticle ink studied by thermoreflectance (SPIE-Intl Soc Optical Eng) p 28

[26] Rahman M, Shahzadeh M and Pisana S 2019 Simultaneous measurement of anisotropic thermal conductivity and thermal boundary conductance of 2-dimensional materials *Journal of Applied Physics* **126** 205103

[27] Schmidt A J, Cheaito R and Chiesa M 2009 A frequency-domain thermoreflectance method for the characterization of thermal properties *Review of Scientific Instruments* **80**

